Modelling Crab-like and Vela-like Pulsars and their Nebulae

T M Nyambe[1], C Venter[1,2], B W Stappers[3], and AK Harding [4]

[1] Centre for Space Research, North-West University, Private Bag X6001, Potchefstroom 2520, South Africa
[2] National Institute for Theoretical and Computational Sciences (NITheCS), Potchefstroom, 2520, South Africa
[3] Jodrell Bank Centre for Astrophysics, University of Manchester, Manchester M13 9PL, UK
[4] Theoretical Division, Los Alamos National Laboratory, Los Alamos, NM 58545, USA

E-mail: 31038018@mynwu.ac.za

Abstract. Crab-like and Vela-like pulsars are young, rapidly rotating neutron stars with strong magnetic fields. Their rotational energy powers pulsed radio and gamma-ray emissions, as well as the surrounding pulsar wind nebulae (PWNe). Crab-like pulsars power compact, high-luminosity nebulae and exhibit characteristic features such as phase-aligned radio and gamma-ray light curves, while Vela-like pulsars power more diffuse PWNe and exhibit phase lags between their radio and gamma-ray pulses. We identify a few bright pulsars and recover their geometric parameters, such as the magnetic inclination and viewing angle, by fitting radio polarisation data with the Rotating Vector Model (RVM). Then, we reproduce their joint radio and gamma-ray light curves using the radio Cone, Two-Pole Caustic, and Outer Gap models. This unified radio and gamma-ray modelling approach constrains the pulsar's geometry and helps us to identify the likely regions of particle acceleration within the magnetosphere, laying the foundation for the combined spectral and spatial modelling of their nebulae. Our results demonstrate a reasonable agreement between the models and observations, underscoring the significance of viewing geometry in pulsar emission.

1 Introduction

Pulsars, first discovered in 1967 by Jocelyn Bell and Antony Hewish [1], are rapidly rotating, highly magnetised neutron stars formed from the core collapse of massive stars with mass $> 8M_{\odot}$. Their combined rapid rotation and strong B-field generate a strong electric field, which extracts charged particles from the star's surface and accelerates them to relativistic energies, emitting radiation over most of the electromagnetic spectrum, from radio to gamma rays. Pulsars offer some of the most extreme environments in the universe, making them a valuable tool for studying physics under extreme conditions. A multi-wavelength study of pulsars is crucial because each emission mechanism (e.g., coherent radio emission, synchrotron radiation, or inverse Compton scattering) plausibly occurs in different regions within their magnetosphere and surrounding environment. The diversity in the observed shapes and structures of the pulse light curves across wavebands hints at where and how the radiation is generated within the complex geometric structure of the magnetosphere.

To unravel the dissipation processes as implied by the light curves, there exist emission and geometric models that explain the complex magnetospheric structures and emission mechanisms of pulsars. Each model assumes a different emission location and B-field structure. The Rotating Vector Model (RVM) provides information about the basic geometric structure of the pulsar B-field relative to our line of sight [2]. The model assumes that the radio emission originates from above the polar cap in a narrow region. The radio conal model [3], the Two-Pole Caustic

(TPC) model [4, 5], and the Outer Gap (OG) model [6, 7], place the radio and high-energy emission regions at specific locations within the magnetosphere. In the high-energy models, acceleration zones form due to the absence of the required charge density (i.e., relatively charge-depleted zones with a charge density lower than the Goldreich-Julian charge density, [8]). The rotational energy lost by the pulsar is converted into pulsed emission, but predominantly into a wind of relativistic particles that powers and shapes the surrounding pulsar wind nebula (PWN).

While research on pulsars has often focused on single-wavelength analysis, our work presents a holistic approach. We aim to build a unified pulsar-PWN framework by integrating the RVM, joint radio and gamma-ray light curve fitting, and PWN modelling. This approach allows us to cross-validate the geometric parameters across the different wavebands. Our objective is to constrain the geometric parameters of our selected Crab-like and Vela-like pulsars using the RVM. Next, we will simulate the radio and gamma-ray light curves based on the radio conal and high-energy (OG, TPC) models and then fit them to the observed data, comparing our results with those found by using the RVM. We will then use the geometric parameters constrained by the radio and gamma-ray models (the magnetic inclination angle α, and the viewing angle ζ) as important inputs to our PWN modelling. We will additionally perform spectral and spatial modelling using a PWN model [9], as well as comparing our geometric constraints with those obtained by independent torus-jet fitting in the literature (e.g., [10]). Our approach in connecting the central pulsar to its extended energetic surrounding environment will follow the method of Maitra et al. [11], who demonstrated the importance of geometric parameter constraints for realistic PWN modelling, also incorporating independent results from jet-torus fitting (e.g., [10]). In this paper, we present our methodology and first results towards a unified understanding of the pulsar-PWN system.

2 Pulsar Sample And Data

The pulsars used for our study are selected based on specific criteria. They must be young ($\tau_{\rm c} < 150$ kyr) and located in the southern hemisphere, a geographical requirement due to the location of the MeerKAT radio telescope. Furthermore, our selection criteria required that our pulsars must have high-quality radio data, characterised by their high signal-to-noise ratio (SNR) and a well-shaped, S-shaped polarisation position angle (PA) curve, in combination with statistically significant gamma-ray pulsed emission, with a well-defined pulse profile. From our selection criteria, we were able to select 10 pulsars that demonstrate clear Crab-like and Vela-like characteristics. Table 1 shows the two examples of pulsars used in this paper. PSR B0301+19 is not included in our main sample due to its older age, but is used separately as a calibration source for our RVM fitting procedure [12]. We selected these types of pulsars because they represent different evolutionary stages and magnetospheric configurations, which offer a valuable study for our integrated approach. We used high-quality gamma-ray data from the Third *Fermi* Pulsar Catalogue (3PC)[1], which contains data from 14 years of on-orbit observations from the *Fermi*-LAT [13]. The radio data used here are obtained exclusively from public archives such as the Australia Telescope National Facility (ATNF)[2] and the European Pulsar Network (EPN)[3] Data Archive and are well calibrated with established timing solutions.

PSR Name	P (s)	$\tau_{\rm c}$ (kyr)	Distance (kpc)	$B_{\rm s}$ (10^{12} G)	$\dot{E}_{\rm rot}$ (ergs/s)
B0301+19 (calibration source)	1.4	17000	0.749	1.36	1.9×10^{31}
J0835−4510 (Vela)	0.09	11.3	0.280	3.38	6.9×10^{36}

Table 1: The parameters for two representative pulsars: period P, characteristic age $\tau_{\rm c} = P/(2\dot{P})$, distance, surface dipole field $B_{\rm s} = 3.2 \times 10^{19}\sqrt{P\dot{P}}$, and spin-down power $\dot{E}_{\rm rot}$.

3 Method

3.1 Radio Emission Geometry: RVM

To understand pulsar emission, one must first understand the geometry of its B-field. The RVM [2] describes the observed radio PA swing as a function of pulse Φ by assuming the magnetic dipole is rotating, while approximating

[1] `https://fermi.gsfc.nasa.gov/ssc/data/access/lat/3rd_PSR_catalog/`

[2] `https://www.atnf.csiro.au/research/pulsar/psrcat/`

[3] `https://psrweb.jb.man.ac.uk/epndb/`

the field structure as that of a static, non-retarded dipole in vacuum:

$$\Psi = \Psi_0 + \arctan\left(\frac{\sin\alpha\sin(\Phi-\Phi_0)}{\sin(\alpha+\beta)\cos\alpha - \cos(\alpha+\beta)\sin\alpha\cos(\Phi-\Phi_0)}\right),$$

where $\Psi(\Phi)$ is the observed PA, Ψ_0 is the reference position angle at the fiducial plane (phase Φ_0), α is the magnetic inclination angle, and β is the smallest angle (impact angle) between the magnetic axis and the observer's line of sight ζ.

Our RVM fitting process involved several steps we implemented in Python. We first extracted the Stokes parameters (I, Q, U, V) from our data and then debiased the linear polarisation (L) using the method explained in Everett et al. [12]. In cases where our PA was discontinuous, we inserted a 90° angle to account for different emission modes, as the classic RVM does not account for such cases. With our PA continuous, we performed a χ^2 minimisation to fit the RVM to the PA curve of our pulsar, using Python's Scipy curve fit function[4].

The parameters α and β are covariant, and if there are not enough data points, the solution may converge to a local minimum. To avoid this, we implemented a two-step fit strategy. First, we performed a χ^2 grid search and obtained robust initial guesses for our parameters α and β. Then, we used our optimised initial guess with the curve fit function, employing the Levenberg-Marquardt algorithm for our final fit [14].

3.2 Radio and Gamma-ray Light Curve Simulations

For our simulations, we used a geometric modelling code that uses various magnetospheric gap geometries, and assumed constant emissivity in the corotating frame [15, 3, 5]. Our simulation focused on the conal radio model, as well as the TPC and OG gamma-ray models. Each model predicts a different region of emission within the magnetosphere. Charged particles are extracted from the surface and accelerated to relativistic energies by the unscreened electric field. These charged particles emit gamma-ray photons via curvature radiation and interact with the intense B-field above the polar caps, producing electron-positron pairs that initiate a cascade. Gaps or charge-depleted regions act as accelerators of particles within the magnetosphere. The radio conal model places the radio emission at a low altitude above the stellar surface.

The TPC places the acceleration region along the last open B-field lines and stretches from the stellar surface to nearly up to the light cylinder. The accelerated charged particles produce caustics when the emission from different altitudes overlaps in phase, resulting in double-peaked light curves with bridge emission. The OG model places the acceleration gap above the null charge surface, where the Goldreich-Julian charge density changes sign, and extends outwards towards the light cylinder. We generate simulations of radio and gamma-ray light curves across a range of α and ζ values. These model light curves are then fit to observed ones by minimising the χ^2 statistic, following the method described by Seyffert et al. [16] to constrain the parameters α and ζ. By jointly fitting radio and gamma-ray light curves, one may potentially obtain stronger constraints.

4 Results

4.1 Radio RVM Fit Results: PSR B0301+19

Investigator	$\alpha\,[^\circ]$	$\beta\,[^\circ]$	$\psi_0\,[^\circ]$	$\phi_0\,[^\circ]$	χ^2_ν
This work	68.56 ± 18.39	2.86 ± 0.41	120.16 ± 0.65	-3.49 ± 0.06	1.62
Everett & Weisberg (2001)[12]	162.0 ± 11.8	0.96 ± 0.63	–	-3.71 ± 0.006	15.6
Blaskiewicz et al. (1991)[17]	69 ± 16	2.9 ± 0.3	–	–	1.42

Table 2: Comparison of RVM fit parameters for PSR B0301+19: our results, those of [12], and the relativistic RVM of [17]. The dashes indicates that the original paper did not report those parameters.

Our RVM fitting produced well-constrained geometric parameters (α, β, Ψ_0, and Φ_0) for PSR B0301+19. The results of our best-fit parameters are presented in Table 2 along with the associated uncertainties and the goodness-of-fit value χ^2_ν. Our results in Table 2 are compared with the results of other investigators on the same pulsar.

[4] `https://docs.scipy.org/doc/scipy/reference/generated/scipy.optimize.curve_fit.html`

Figure 1 shows the radio pulse profile observed for PSR B0301+19. The top panel displays the averaged pulse profile, and the bottom panel shows the polarisation PA (blue) with the best-fit RVM curve (red), indicating a reasonable fit. The derived values of α, β, and Ψ_0 show some consistency with previous studies of the same pulsar. Although the values of α and Φ_0 are close and our χ^2_ν is reasonably close to 1, the α of Everett and Weisberg seems very different. Even $180^\circ - \alpha = 18^\circ$ is different from 69°. This may be due to data quality issues that they encountered. In addition, differences in the fitting method, such as the fraction of the pulse phase they used, may also play a role.

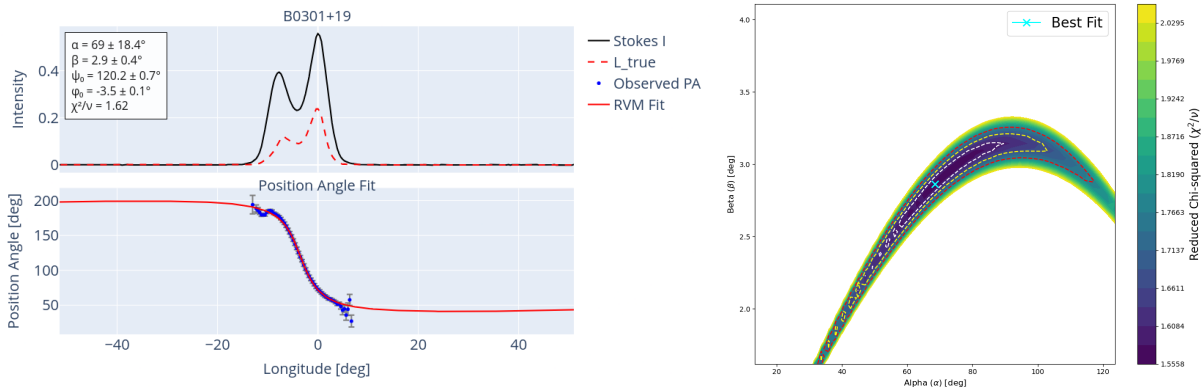

Figure 1: Plot of the RVM fitting for PSR B0301+19. The left panel displays the pulsar profile in Stokes parameters, intensity (black) and linear polarisation (red dashed). The PA is in blue, and the best-fit RVM is in red in the bottom left panel. The right panel displays the α-β plane. The image is a χ^2 contour plot, with the blue cross representing the best fit for B0301+19. The contours represent the 1σ, 2σ, and 3σ confidence regions for the fitted parameters (α and ζ), based on standard $\Delta\chi^2$ values of 2.30, 6.18, and 11.83, respectively, for a two-parameter fit [18].

4.2 Initial Radio And Gamma-ray Light Curve Simulations: PSR J0835-4510

Figure 2 shows the radio and gamma-ray light curves generated by our simulation for the radio cone, the TPC, and the OG models. In our simulation, with geometry of $\zeta = 90^\circ$, the models always predict a gamma-ray peak separation of 0.5, which does not match the observed phase separation of 0.4. So our simulations are illustrative examples, not fits to the actual data. The fitting of our simulated light curves to the observed data will be presented in future work.

5 Conclusion

In this paper, we presented the methodology and initial results of a novel, multi-wavelength study of pulsar emission, integrating the radio RVM with joint radio and gamma-ray light curve simulations. Our application of the RVM to PSR B0301+19 has yielded geometric parameters of α and β that are consistent with the RVM modelling of other investigators. The difference in our results is due to the differing data quality and fitting method used by us and by them. We will next deploy our code to our sample of selected pulsars. We have also successfully produced the radio and gamma-ray light curves using the set of magnetospheric models (conal radio, TPC, and OG), and we have begun the process of jointly fitting these simulations to observed radio and *Fermi*-LAT data, thereby constraining the high-energy emission geometry. Our unified approach promises a direct comparison of the geometric parameters derived from the different wavebands and geometric models, which will offer us better insights into the complex magnetospheric structure and emission mechanisms of the pulsar-PWN system.

6 Future Work

In the future, we will focus on completing the fitting of our RVM and the simulated radio and gamma-ray light curves to the full observed dataset of our entire pulsar sample. Following this, we will apply a PWN model [9, 19] to model spectral and spatial data. We will also use published fitting results from the jet-torus PWN model to further constrain our model parameters. While our gamma-ray models are slightly dated, we use them to demonstrate our methodology, since they are computationally inexpensive and they produce skymaps (intensity vs. observer angle

and phase) that are similar to those of the more expensive current sheet models. In future, we will implement a geometric current sheet model (e.g., [20]) and compare the resulting gamma-ray light curve predictions with our current results. Our approach will be applied comparatively to Crab-like and Vela-like pulsars, which will contribute to our understanding of the complete pulsar-PWN system, bridging the gap between the energy supplier and its extended nebula.

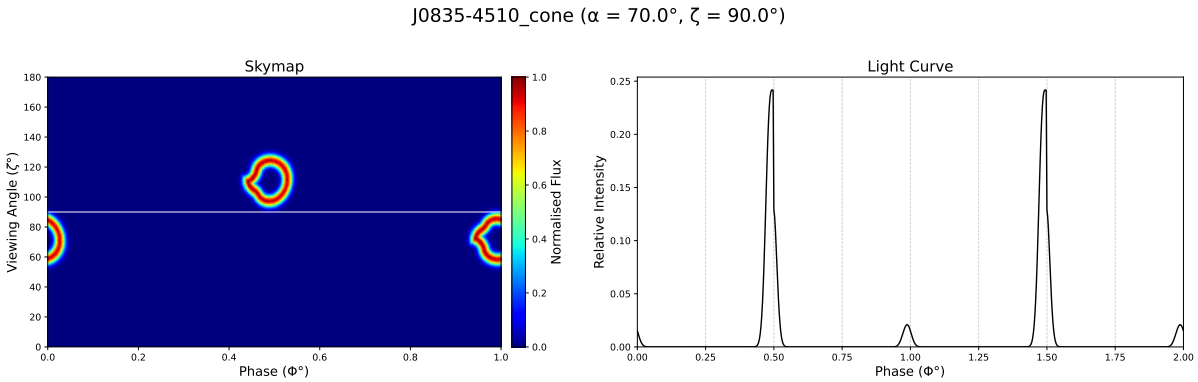

(a) Illustrative radio conal model of PSR J0835-4510 at $\alpha = 70^\circ$, $\zeta = 90^\circ$.

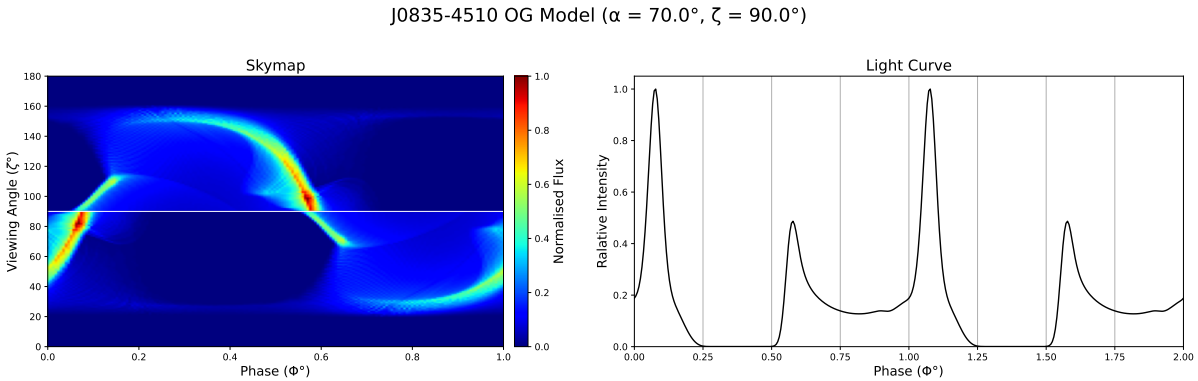

(b) OG model of PSR J0835-4510 with same geometry as Fig. 2a.

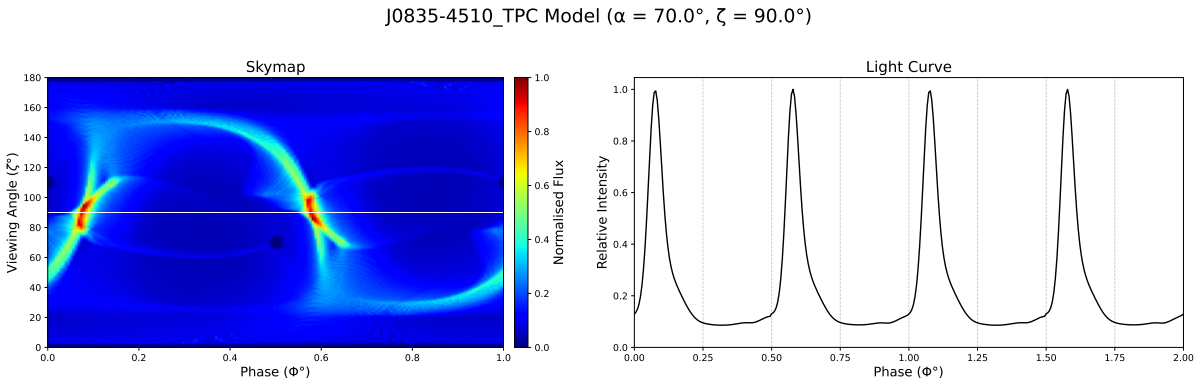

(c) TPC model of PSR J0835-4510 with same geometry as Fig. 2a.

Figure 2: Simulated phaseplots (left) and light curves (right) for PSR J0835-4510 under one radio and two gamma-ray models: (a) radio conal, (b) OG, and (c) TPC, all at $\alpha = 70^\circ$, $\zeta = 90^\circ$. The light curves are simulated to show two full rotations for clarity.

References

[1] A. Hewish, S. J. Bell, J. D. H. Pilkington, P. F. Scott, and R. A. Collins, "Observation of a Rapidly Pulsating Radio Source," *Nature*, vol. 217, no. 5130, pp. 709–713, Feb. 1968.

[2] V. Radhakrishnan and D. J. Cooke, "Magnetic Poles and the Polarization Structure of Pulsar Radiation," *Astrophys. Lett.*, vol. 3, p. 225, Jan. 1969.

[3] S. A. Story, P. L. Gonthier, and A. K. Harding, "Population Synthesis of Radio and γ-Ray Millisecond Pulsars from the Galactic Disk," *ApJ*, vol. 671, no. 1, pp. 713–726, Dec. 2007.

[4] J. Dyks and B. Rudak, "Two-Pole Caustic Model for High-Energy Light Curves of Pulsars," *ApJ*, vol. 598, no. 2, pp. 1201–1206, Dec. 2003.

[5] C. Venter, A. K. Harding, and L. Guillemot, "Probing Millisecond Pulsar Emission Geometry Using Light Curves from the *Fermi*/Large Area Telescope," *ApJ*, vol. 707, no. 1, pp. 800–822, Dec. 2009.

[6] K. S. Cheng, C. Ho, and M. Ruderman, "Energetic Radiation from Rapidly Spinning Pulsars. I. Outer Magnetosphere Gaps," *ApJ*, vol. 300, p. 500, Jan. 1986.

[7] R. W. Romani, "Gamma-Ray Pulsars: Radiation Processes in the Outer Magnetosphere," *ApJ*, vol. 470, p. 469, Oct. 1996.

[8] P. Goldreich and W. H. Julian, "Pulsar Electrodynamics," *ApJ*, vol. 157, p. 869, Aug. 1969.

[9] C. van Rensburg, C. Venter, A. S. Seyffert, and A. K. Harding, "Exploiting morphological data from Pulsar Wind Nebulae via a spatiotemporal leptonic transport code," *MNRAS*, vol. 492, no. 3, pp. 3091–3102, Mar. 2020.

[10] C. Y. Ng and R. W. Romani, "Fitting Pulsar Wind Tori," *ApJ*, vol. 601, no. 1, pp. 479–484, Jan. 2004.

[11] C. Maitra, F. Acero, and C. Venter, "Constraining the geometry of PSR J0855-4644: A nearby pulsar wind nebula with double torus/jet morphology," *A&A*, vol. 597, p. A75, Jan. 2017.

[12] J. E. Everett and J. M. Weisberg, "Emission Beam Geometry of Selected Pulsars Derived from Average Pulse Polarization Data," *ApJ*, vol. 553, no. 1, pp. 341–357, May 2001.

[13] B. Limyansky, "The Third *Fermi* Pulsar Catalog," in *AAS/High Energy Astrophysics Division*, ser. AAS/High Energy Astrophysics Division, vol. 17, Mar. 2019, p. 109.32.

[14] J. J. Moré, "The Levenberg-Marquardt algorithm: Implementation and theory," in *Lecture Notes in Mathematics, Berlin Springer Verlag*, 1978, vol. 630, pp. 105–116.

[15] J. Dyks, A. K. Harding, and B. Rudak, "Relativistic Effects and Polarization in Three High-Energy Pulsar Models," *ApJ*, vol. 606, no. 2, pp. 1125–1142, May 2004.

[16] A. S. Seyffert, C. Venter, A. K. Harding, J. Allison, and W. D. Schutte, "Implementation of a goodness-of-fit test for finding optimal concurrent radio and gamma-ray pulsar light curves," *arXiv e-prints*, p. arXiv:1611.01076, Nov. 2016.

[17] M. Blaskiewicz, J. M. Cordes, and I. Wasserman, "A Relativistic Model of Pulsar Polarization," *ApJ*, vol. 370, p. 643, Apr. 1991.

[18] P. R. Bevington and D. K. Robinson, *Data reduction and error analysis for the physical sciences*, 2003.

[19] A. Kundu, J. C. Joshi, C. Venter, N. E. Engelbrecht, W. Zhang, D. F. Torres, I. Sushch, and S. J. Tanaka, "Spatio-spectral-temporal modelling of two young pulsar wind nebulae," *MNRAS*, vol. 535, no. 3, pp. 2415–2435, Dec. 2024.

[20] J. Pétri, "Multi-wavelength pulse profiles from the force-free neutron star magnetosphere," *A&A*, vol. 687, p. A169, Jul. 2024.